Journal of Non-Crystalline Solids xxx (xxxx) xxxx

Contents lists available at ScienceDirect

Journal of Non-Crystalline Solids

journal homepage: www.elsevier.com/locate/jnoncrysol

Structural evolution of fused silica below the glass-transition temperature revealed by in-situ neutron total scattering

Ying Shi[a,*], Dong Ma[b], Albert P. Song[c], Bryan Wheaton[a], Mathieu Bauchy[d], Stephen R. Elliott[e]

[a] Science and Technology Division, Corning Incorporated, Corning, NY 14831, USA
[b] Neutron Science Platform, Songshan Lake Materials Laboratory, Dongguan, Guangdong 523808, China
[c] Corning-Painted Post High School, Corning, NY 14830, USA
[d] Physics of AmoRphous and Inorganic Solids Laboratory (PARISlab), Department of Civil and Environmental Engineering, University of California, Los Angeles, CA 90095, USA
[e] Department of Chemistry, University of Cambridge, Lensfield Road, Cambridge CB2 1EW, UK

ARTICLE INFO

Keywords:
In-situ neutron total scattering
Structural change of fused silica
Short- and medium-range structure
First sharp diffraction peak
Rigid-unit mode

ABSTRACT

The common belief that glass structure is completely frozen-in at room temperature is challenged at both macroscopic and atomic scales. Here, we demonstrate an analytical method to elucidate the fine details of a continuous structural change of fused silica (FS) at temperatures below the glass-transition temperature using *in-situ* neutron total scattering. We find that the SiO_4 tetrahedron expands through the entire temperature range with a local coefficient of thermal expansion of 9.1×10^{-6} K^{-1}, while the average medium-range distance, derived from the first sharp diffraction peak of the structure factor, expands at a rate of 21×10^{-6} K^{-1}. Such an expansion difference reflects glass-structure changes within the "rigid-unit mode" model, where each tetrahedron behaves as a rigid unit and the flexible rotations between rigid units lead to more than two times higher medium-range thermal expansion. We further demonstrate that such rotations change the shape of individual rings, leading to a measurable change in the first sharp diffraction peak (FSDP). This study paves the way to measure the structural changes of other silicate glasses, especially through the glass transition.

1. Introduction

It is commonly believed that glass structure is frozen at room temperature. Viscous flow of medieval cathedral glass is a debunked urban legend and has been quantified to be too slow to be measurable [1]. However, this view is challenged at both macroscopic and atomic scales. The very first glass-aging phenomenon, referred to as the "thermometer effect" [2], was reported in the nineteenth century [3], where the ice-point reading drifted over a period of forty five years due to the glass dimensional change. A well-controlled room-temperature dimensional measurement of an industrial silicate glass showed a 10 parts per million (ppm) shrinkage over a 1.5 year period, corresponding to a daily change of 18 parts per billion (ppb) [4]. Fused silica (FS), considered as a stable glass, also showed a 0.5 ppb compaction per day [5]. X-ray photon correlation spectroscopy (XPCS) has directly revealed the existence of some structural rearrangements in sodium silicate glass on a length scale of 3–7 Å within a few minutes, at a temperature far below T_g [6]. In conclusion, the glass structure can change at low T.

The low-T glass relaxation can only be induced by low-energy structural deformations, which most likely represent conformational changes of rings without bond breakage, similar to those observed in crystalline polymorphs of SiO_2. The most obvious candidate for such low-energy structural deformations is the flexible rotations of SiO_4 rigid units, defined as the rigid-unit mode (RUM) for framework silicate crystals [7,8]. The basic idea of the rigid unit is that the intra-SiO_4 tetrahedral forces (Si-O stretching and O-Si-O bending) are much stronger than the inter-tetrahedral forces (the corner-linked Si-O-Si torsion). A very high-energy penalty is required to distort a tetrahedron; therefore, it should be treated as a rigid unit. Instead, low-energy deformations are achieved by the Si-O-Si rotation, including both bond-

* Corresponding author.
E-mail address: shiy3@corning.com (Y. Shi).

https://doi.org/10.1016/j.jnoncrysol.2019.119760
Received 29 August 2019; Received in revised form 21 October 2019; Accepted 29 October 2019

angle and dihedral torsion-angle changes. For both silicate glasses and crystals, RUMs can be calculated by molecular-dynamics simulations with a RUM analysis [8–11], and have been experimentally observed by inelastic-neutron total-scattering measurements [12]. The RUM model was originally developed to explain the displacive phase transitions of crystalline framework silicates [7,8]. A rigid-unit-mode (RUM) study showed that the α→β quartz phase transition involves Si-O-Si rotations with a preserved bond angle [8]; the torsion between rigid SiO_4 units through flexible Si-O-Si rotations occurs through the whole temperature range, underlying the dynamic disorder [13].

Later, RUM theory was expanded to silicate glasses, in which RUMs are called “floppy modes” [14]. The floppy modes are low-energy deformations composed of linked rigid units, and can propagate, with these rigid units rotating relative to each other without distorting. Further molecular-dynamics simulations and RUM analyses [10] confirmed the same flexibility in the glass as in the crystal, which allows the glass structure to undergo large spontaneous changes through reorientations of the SiO_4 tetrahedra with a very low-energy cost. Therefore, we use RUM theory to address the physical origin of the relaxation of the glass structure below the glass-transition temperature, a challenging unsolved problem with both fundamental and practical importance. During the same time frame (2000) when the RUM model was applied to silicate glasses, Nemilov already proposed the same idea as ours today, albeit not using the RUM terminology. He attributed the structural origin of low-T relaxation, also called β-relaxation, to the displacive movement of bridging oxygen atoms (O in the Si-O-Si bonding) [15].

In this study, we try to reveal “how glass structure changes with rigid-unit-mode behavior” using *in-situ* neutron total scattering for FS glass. We demonstrate two analytical methods to elucidate the fine details of the continuous structural change of FS from room temperature to 950 °C. The short-range structural information is derived from the nearest Si-O and O-O atom pairs of the pair distribution function in real space. The medium-range structural information is derived from the first sharp diffraction peak (FSDP) of the structure factor in reciprocal space. Both nearest Si-O and O-O atom pairs, which form the basic building block, the SiO_4 tetrahedron, show similar local coefficients of thermal expansion (CTE) of 9.1×10^{-6} K^{-1}, indicating that the tetrahedron is relatively rigid. In contrast, the average medium-range distance expands with a CTE of 21×10^{-6} K^{-1}, reflecting the flexible rotations between tetrahedra, which lead to a more than two times higher expansion in the medium range. Such rigid SiO_4-unit torsion by flexible Si-O-Si angle rotation leads to nearest-tetrahedra rearrangements, which eventually causes a change in the shape of the silicate rings in the medium range. This is reflected in the subtle but noticeable area and shape change of the first sharp diffraction peak (FSDP). Using the newly developed RingFSDP method [16], the ring-structure evolution with temperature can be quantified. This method paves the way to study through-T_g structural changes of other silicate glasses.

2. Experimental

Fused silica 7940 was core-drilled into a 6 mm diameter and 24 mm long rod. The glass rod was loaded into a vanadium can, and heated in an ILL furnace with a 5 °C/min ramping rate with a staircase profile, from room temperature to 950 °C. At each data-collection temperature, the sample was held isothermally for 25 min, which included 5 min of hold time followed by 20 min of data collection. A room-temperature scan was conducted first, the 20-minute scan was performed at every 150 °C interval until 750 °C, and then with 10°C–25 °C intervals till 950 °C. Time-of-flight (TOF) neutron-scattering measurements were performed on the Nanoscale-Ordered Materials Diffractometer (NOMAD) at the Spallation Neutron Source (SNS), Oak Ridge National Laboratory [17]. All the structure factors used in this study were normalized to an absolute scale utilizing the low-r region of $G(r)$ criterion, as described in [18].

3. Results

3.1. . In situ high-temperature neutron total scattering

As a prototypical network-forming glass, the temperature-induced structural change of FS has been studied by *in-situ* neutron [19,20] and X-ray [21,22] total-scattering analyses. Although each study has its own focus, two common structural changes are determined as the temperature increases: as a result of thermal vibration, the nearest-neighbor Si-O bond length increases and the peak area of the first sharp diffraction peak (FSDP) decreases. A little-noticed detail is a small shoulder that forms on the low-Q side of the third peak in the neutron structure factor at around 4.5 $Å^{-1}$, which corresponds to the second peak in the X-ray $S(Q)$. This shoulder formation is clearly exhibited in the $S(Q)$ figures of all papers, but is only mentioned in the X-ray studies without further explanation [21,22]. Similarly, this shoulder is also present in the *in-situ* neutron $S(Q)$'s of more complicated soda-lime glasses [23].

The reduced structure factor, $F(Q)$ ($F(Q) = Q[S(Q) - 1]$), of FS as a function of temperature is presented in Fig. 1. The statistical errors of the measured data points in $F(Q)$ for RT and 950 °C glasses are plotted in the Extended Data Fig. 1. The statistic errors are relatively low for the low-Q range but significantly increase for the high-Q range, especially at 950 °C. As described below, we only use the low-Q FSDP to derive the medium-range structure information, so that the high errors in high-Q range do not significantly affect our analytical accuracy. Moreover, according to the general practice in the diffraction field for crystalline materials, such statistical errors are not propagated during further analyses from peak fitting, such as lattice constants, crystallite size, or residual stress determination.

As shown in Fig. 1, beyond about 4 $Å^{-1}$ the structure factor is dominated by the two sharpest Fourier components representing the intra-tetrahedron Si-O and O-O correlations. As temperature increases, the O-O correlation broadens faster than the Si-O correlation. This behavior is to be expected, since the O-atoms are separated by two Si-O bonds. As explained in Section 3.2.2, the observed changes in $S(Q)$ are reflective of that, leading in particular to the formation of the shoulder at 4.5 $Å^{-1}$, as shown in the insert of Fig. 1.

The reduced pair distribution functions, $G(r)$, obtained by direct Fourier transformation of $F(Q)$, with $G(\boldsymbol{r}) = (\frac{2}{\pi}) \int_0^{Q_{max}} \boldsymbol{F}(\boldsymbol{Q})\sin(\boldsymbol{Qr})\boldsymbol{dQ}$

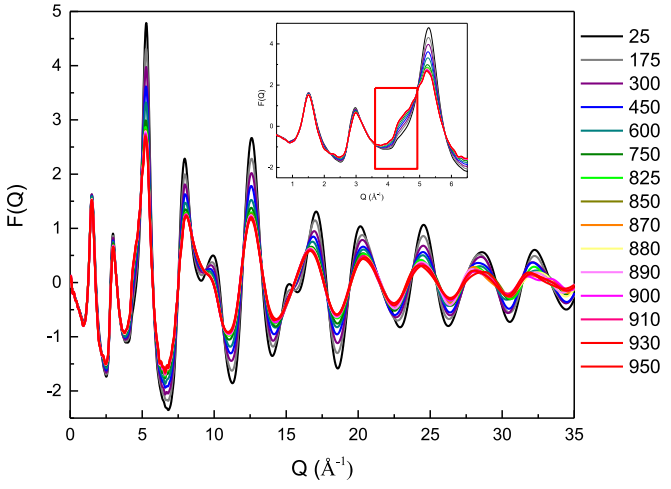

Fig. 1. Reduced structure factor functions, F(Q), of FS glass measured at different temperatures. Insert: zoomed first three low-Q peaks, with the 4.5 $Å^{-1}$ shoulder formation highlighted by the red rectangle. (For interpretation of the references to color in this figure legend, the reader is referred to the web version of this article.)

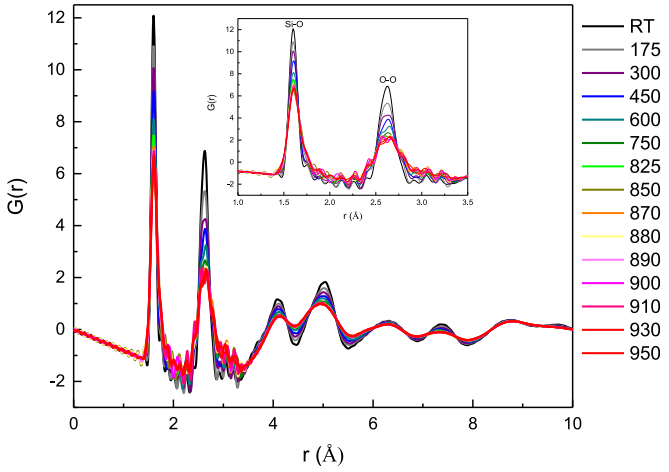

Fig. 2. Reduced pair distribution functions G(r) of FS glass obtained by Fourier transformation with Q_{max} = 50 Å^{-1}. Insert: zoomed Si-O and O-O peaks show broadening as well as a long-tail formation on the high-*r* side as the temperature increases.

(Q_{max} = 50 Å^{-1}), are shown in Fig. 2. The Fourier transform propagation error for RT and 950 °C glasses is plotted in the Extended Data Fig. 2. Similar to *F(Q)*, the *G(r)* errors are relatively low for the low-*r* range but significantly increase for the high-*r* range, especially at 950 °C. Since we only use the first two low-*r* peaks (Si-O and O-O atom-pair correlation) to derive the short-range structure information, the high errors in high-*r* range do not significantly affect our analytical accuracy. Again the Fourier transformation errors are not propagated during the further peak fitting as described in Section 3.2.2.

The nearest-neighbor Si-O correlation is asymmetric with a long-*r* tail, indicating that some Si-O bonds are under strain. The asymmetry might also be caused by a second small high-*r* peak or/and anharmonicity. The average oxygen coordination number around silicon atoms, n_{Si}^{O}, obtained from integration of the first Si-O peak in the radial distribution function, *R(r)* ($R(r) = 4\pi r^2\rho_0 + rG(r)$, with ρ_0 being the number density) [24], is 4.1 ± 0.2 for all temperatures, indicating that the SiO_4 tetrahedra remain intact.

3.2. . Method I: tetrahedron expansion for short-range structure

3.2.1. . Reciprocal-space representation of intra-tetrahedral bonds – $I_{Si\text{-}O}(Q)$ and $I_{O\text{-}O}(Q)$

As shown in the insert of Fig. 2, both nearest-neighbor peaks from Si-O and O-O correlations become broader and asymmetrical as the temperature increases. As demonstrated in Extended Data Fig. 1, direct peak fitting of *T(r)* ($T(r) = 4\pi r\rho_0 + G(r)$) can be used to derive correct mean-square atom-pair distance deviation $<u_{Si-O}^2>$ values that match with reported data [20], but give two times higher $\langle u_{O-O}^2\rangle$ values at elevated temperatures. To derive accurate structural information, we choose to work with the reciprocal-space representation of atom-pair correlations since it expands the signal and allows for more reliable model fitting, as demonstrated in our RingFSDP method [16].

Since our Fourier transformation algorithm only allows us to compute the Fourier transformation of *G(r)* over the entire range of *r* values rather than over the extent of the individual single peaks of *G(r)*, we use the following procedure to derive the reciprocal-space representation, $I(Q)_{Si\text{-}O}$, for the nearest-neighbor Si-O atom pairs in *G(r)*. As shown in Fig. 3(a), *G(r)* (red curve) can be decomposed into two additive components: the Si-O nearest-neighbor peak itself, shown in black, and everything else, denoted as *G′(r)* and shown in blue. Fourier transformation of *G(r)* and *G′(r)* leads to the corresponding reduced structure factors, *F(Q)* and *F′(Q)*, with $F(Q) = \int_0^{Q_{max}} G(r)\sin(Qr)dr$. As shown in Fig. 3(b), $I_{Si\text{-}O}(Q)$ is the difference between *F′(Q)* and *F(Q)*, shown as the black dot curve. It is mathematically equivalent to the direct Fourier transformation of the nearest-neighbor Si-O atom pairs. $I_{Si\text{-}O}(Q)$ appears as a decaying sine wave and it matches perfectly with *F(Q)* (red) in the region of $Q \geq 22.5$ Å^{-1}, indicating that this region is determined by the short-range Si-O bonds. The same procedure, as illustrated in Fig. 3(c) and (d), is applied to obtain $I_{O\text{-}O}(Q)$ for the first O-O atom pairs.

3.2.2. . Fitting for atom-pair lengths and DW factors

To quantify the atom-pair length and DW factor, we use the equations that describe the contribution of a single atomic pair, *ij*, to the partial correlation function, $G_{ij}(r)$, in real-space (Eq. (1)) [25].

Assuming that an atomic pair, *ij*, has a Gaussian distribution, with a mean value r_{ij} and a root-mean-square (RMS) deviation in distance, $\langle u_{ij}^2\rangle^{1/2}$, its contribution to the weighted partial correlation function $T_{ij}(r)$ ($T(r) = 4\pi r\rho_0 + G(r)$) is given by Eq. (1):

$$T_{ij}(r) = \frac{n_i^j \times B_{ij}/c_i}{r_{ij}\sqrt{2\pi}\langle u_{ij}^2\rangle^{1/2}} \exp\left[-\frac{(r-r_{ij})^2}{2u_{ij}^2}\right] \quad (1)$$

The n_i^j are coordination numbers, which are the number of atoms of type *j* around atoms of type *i*, and $B_{ij} = \frac{c_i c_j b_i b_j}{(\sum c_i b_i)^2}$ with c_i and b_i being the atomic fraction and neutron-scattering length of chemical species *i*, respectively.

The contribution of the same atomic pair described in Eq. (1) to the reduced total structure factor, $I_{ij}(Q)$, is represented by Eq. (2):

$$I_i j(Q) = \frac{n_i^j \times B_{ij}/c_i}{r_{ij}}\sin(r_{ij}Q)\exp(-Q^2 < u_{ij}^2 > /2) \quad (2)$$

Eqs. (1) and (2) illustrate the same physical origin - a Gaussian-shaped atomic-pair correlation, *ij*, in different spaces. They contain exactly the same structural information; therefore, fitting in reciprocal space does not solve the high-*T* asymmetric, non-Gaussian peak-shape issue. Theoretically, fitting either a single Gaussian peak in *T(r)* or a decaying sine wave in *I(Q)* should provide the same structural values, r_{ij}, $\langle u_{ij}^2\rangle$ and n_i^j. However, the two Gaussian peak-fitting parameters, width ($\langle u_{ij}^2\rangle^{1/2}$) and area ($n_i^j$), are often highly correlated with each other, leading to unreliable fitting, as shown by the unphysically high $\langle u_{O-O}^2\rangle$ values at high temperature plotted in Extended Data Fig. 3. In contrast, the Fourier-transformed *I(Q)* expands the signal and separates the $\langle u_{ij}^2\rangle^{1/2}$ factor from n_i^j, where n_i^j is directly determined by the height of the first sine peak and $\langle u_{ij}^2\rangle$ is the decay rate of the sine wave. It should be noted that the n_i^j determined from the *I(Q)* fitting is heavily affected by the *r*-range chosen for the $G(r)_{ij}$→$I(Q)_{ij}$ transformation; therefore, it should not be used for coordination-number calculations. The best practice to determine the coordination number from neutron-scattering data is still by the peak integration of *R(r)*, as stated in [26].

The advantage of fitting *I(Q)* instead of *T(r)* is more discernible for the high-temperature data, where the atomic-pair correlations become more asymmetric and depart from a Gaussian shape. This is demonstrated by the dependency factors of $\langle u_{ij}^2\rangle$ and n_i^j generated from fitting. The dependency factor reflects the correlation between two fitting parameters and has a value from zero to one [27]. The higher the value, the more is the derived parameter correlated with the other fitting parameter and is less reliable. For the $T_{Si\text{-}O}(r)$ single-peak fitting, the RT dependency factors of $\langle u_{ij}^2\rangle$ and n_i^j are 0.452 and 0.596, respectively; they increase to 0.534 and 0.711, respectively, for the 950 °C data. For the $I_{SiO}(Q)$ decayed sine-wave fitting, the RT dependency factors of $\langle u_{ij}^2\rangle$ and n_i^j are 0.361 and 0.357, respectively; they remain almost unchanged as 0.336 and 0.334, respectively, for the 950 °C data.

The *F(Q)* and *I(Q)* curves of Si-O and O-O atom pairs for FS at four different temperatures are shown in Fig. 4; the fitted curve (dot) matches well with the measured one (solid), and all the *I(Q)* fittings show a reduced mean-square-error $\chi^2 < 0.006$. A Python code "Tetrahedron Expansion" was developed to batch process the *F(Q)* files to obtain *I(Q)* of Si-O and O-O atom pairs and then profile-fit *I(Q)*. As demonstrated in Fig. 4, The *F(Q)* in the range of 4.5 Å^{-1} is contributed by the positive *I*

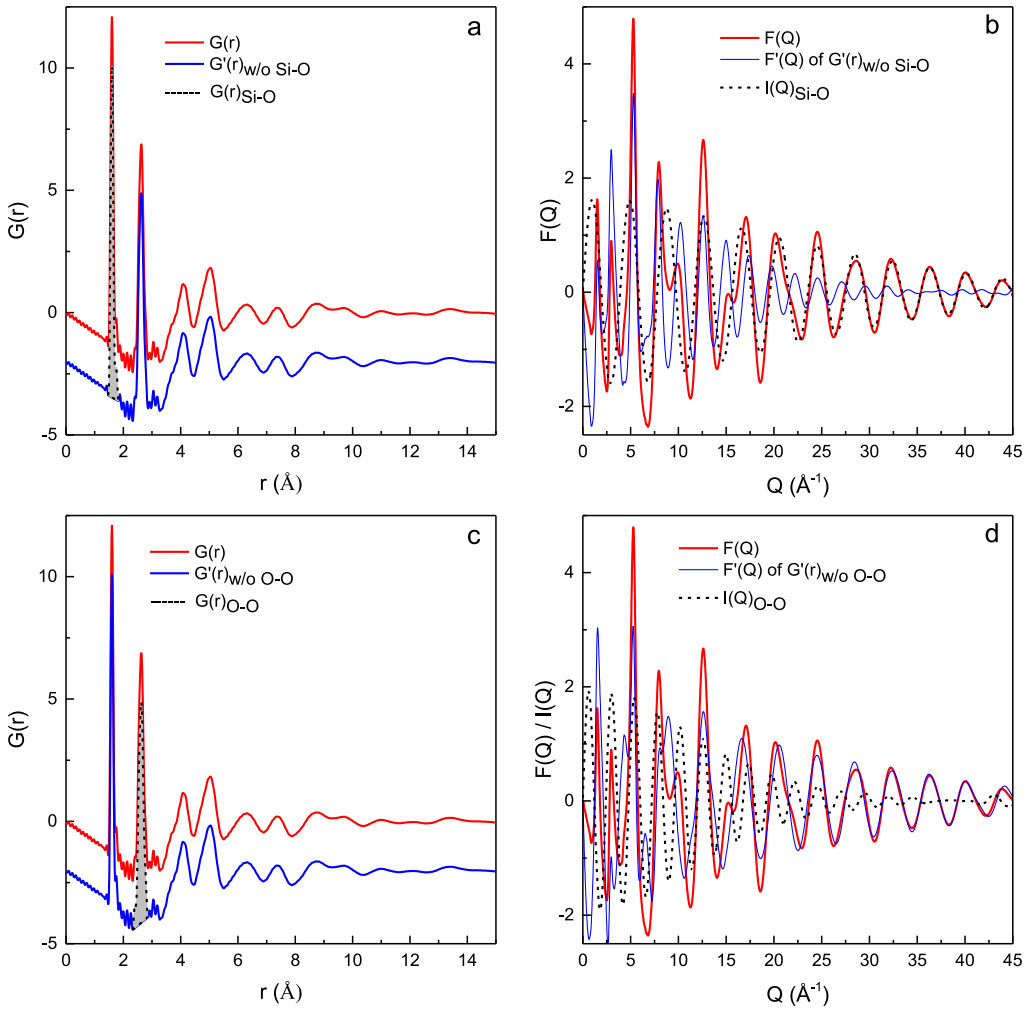

Fig. 3. Reciprocal-space *I(Q)s* obtained by Fourier transformation of $G(r)_{\text{Si-O}}$ and $G(r)_{\text{O-O}}$ for fused silica. (a) Real space: original *G(r)* (red); *G'(r)* with 1st Si-O pair subtracted (blue); $G_{Si\text{-}O}(r)$ (black), both blue and black curves are shifted down by 2 for clarity. (b) Reciprocal space: *F(Q)* of original *G(r)* (red); *F'(Q)* of *G'(r)* (blue); *I (Q)* of 1st Si-O pairs (black), where $I(Q) = F(Q) - F'(Q)$. Same notation for O-O pairs in (c) and (d). (For interpretation of the references to color in this figure legend, the reader is referred to the web version of this article.)

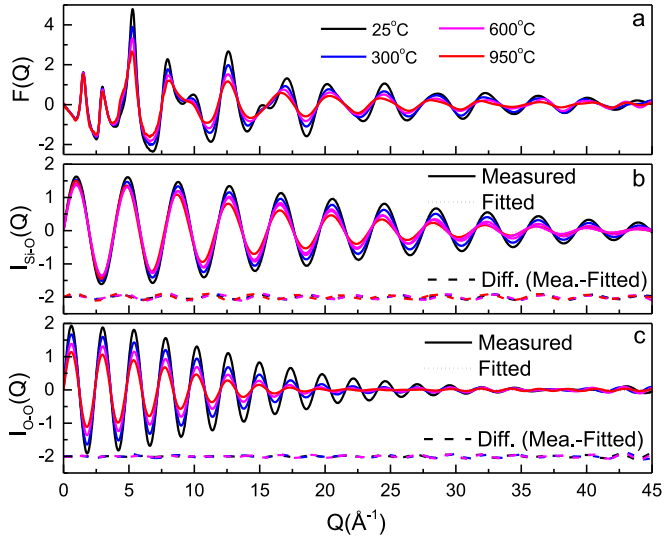

Fig. 4. Structure factor overlay for FS at four temperatures: (a) *F(Q)*; (b) $I(Q)_{\text{Si-O}}$; (c) $I(Q)_{\text{O-O}}$. The measured *I(Q)* curves are shown as solid lines and their fitted data are plotted by dotted curves in (b) & (c); the difference between measured and fitted data (dashed curve) is plotted down by −2 for clarity.

$(Q)_{\text{Si-O}}$ and negative $I(Q)_{\text{O-O}}$. For high-*T* glass, the negative contribution from $I(Q)_{\text{O-O}}$ decays much faster than the decaying of positive Si-O contribution, which leads to a positive shoulder formation compared to RT glass, as marked by the red rectangle in the insert of Fig. 1.

3.2.3. . *SiO₄ tetrahedron expansion*

The Si-O and O-O atom-pair length changes with *T*, derived from *I (Q)* fitting, are plotted in Fig. 5(a) and (b); their thermal expansions are calculated by the expression $Expansion_T = \frac{r_T - r_{RT}}{r_{RT}}$ and are plotted in Fig. 5(c). Both atom pairs show a similar expansion rate, while the O-O data are more scattered than the Si-O data due to the relatively weaker signal. A local coefficient of thermal expansion (CTE), $9.1(9) \times 10^{-6}$ (K^{-1}), is obtained from a linear fitting of the Si-O atom-pair expansion data with the errors calculated from the $I_{\text{Si-O}}(Q)$ fitting result. As explained earlier, the *G(r)* Fourier transformation error is not propagated for the CTE error calculation. We also do not consider any systematic error contribution. First it was minimized by the instrument calibration. Second, in our study, any systematic error (if any) would have the same effect on all the atom-pair distances and, hence, would not change the CTE slope.

The derived CTE value is in the range of reported local CTE results (6–12.6) $\times 10^{-6}$ K^{-1} of various silicate crystalline materials [28]. These values were calculated by a TLS rigid-body analysis, which has been applied to crystal-structure refinements of various silicate phases

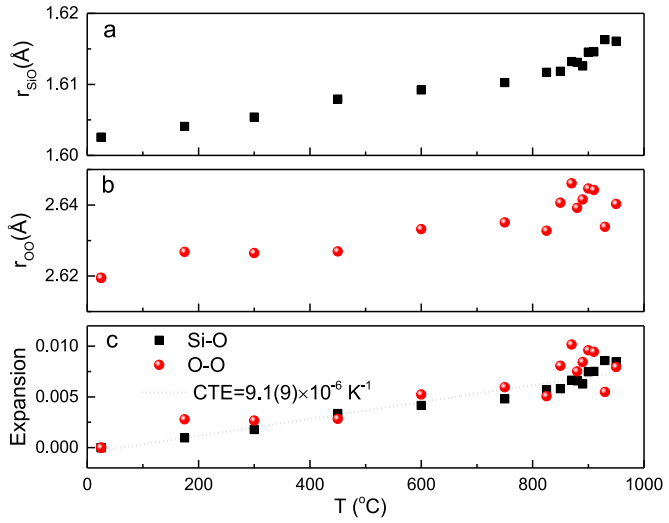

Fig. 5. Temperature dependence of Si-O (a) and O-O (b) atom-pair distances determined by *I(Q)* fitting and their expansions with temperature (c). The fitting error is much smaller than the symbol size. The CTE slope (black dot line) is determined by a linear fitting of Si-O expansion data weighted by the $I_{Si\text{-}O}(Q)$ fitting error.

using Bragg-diffraction data [28]. Our result is larger than the local CTE value determined for SiO_2 crystalline polymorphs, *viz.* $2.2(4) \times 10^{-6}$ K^{-1} [29]. However, it is comparable with Si-O bond CTE values of soda-lime silicate glass ($6(1) \times 10^{-6}$ K^{-1}) [23] and potassium disilicate glass ($9(1) \times 10^{-6}$ K^{-1}) [30], both determined from Si-O bond-length changes measured by neutron scattering.

3.2.4. . Atom-pair distance deviation change

The mean-square atom-pair distance deviations, $\langle u^2_{Si-O}\rangle$ and $\langle u^2_{O-O}\rangle$, are also derived from $I(Q)_{Si\text{-}O}$ and $I(Q)_{O\text{-}O}$ fitting of total scattering data. As shown by the ball symbols in Fig. 6, they increase linearly with temperature. For the same temperature, $\langle u^2_{O-O}\rangle$ is about three to four

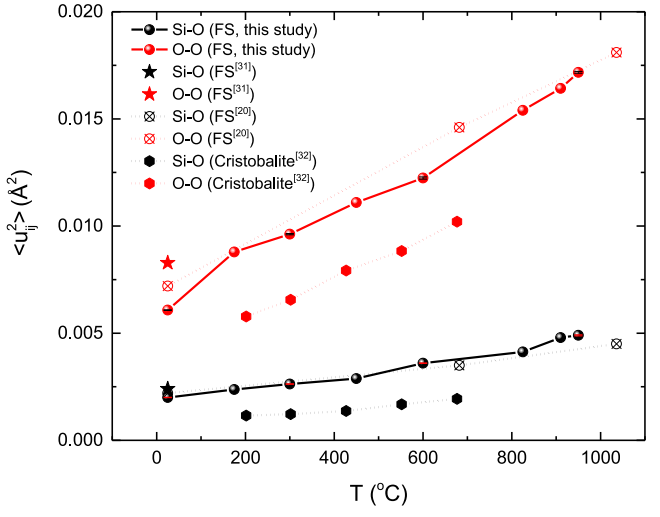

Fig. 6. Mean-square atom pair distance deviation $\langle \boldsymbol{u}^2_{ij}\rangle$ change with temperature of FS and cristobalite, derived from total scattering. The data for Si-O atom pairs are shown in black and for O-O atom pairs in red. The $\langle \boldsymbol{u}^2_{Si-O}\rangle$ (black ball) and $\langle \boldsymbol{u}^2_{O-O}\rangle$ (red ball) of FS are derived from the $I(Q)_{Si\text{-}O}$ and $I(Q)_{O\text{-}O}$ fitting, with error bars (smaller than symbol size) shown for four temperatures. The $\langle \boldsymbol{u}^2_{Si-O}\rangle$ (black hexagon) and $\langle \boldsymbol{u}^2_{O-O}\rangle$ (red hexagon) for cristobalite are from [32]. The RT FS data plotted as star symbols are from Ref. [31], and in-situ FS data plotted as crossed circles are from [20]. (For interpretation of the references to color in this figure legend, the reader is referred to the web version of this article.)

times higher than $\langle u^2_{Si-O}\rangle$.

The *in-situ* [20] as well as room-temperature data [31] $\langle u^2_{Si-O}\rangle$ and $\langle u^2_{O-O}\rangle$ of FS have been measured by neutron total scattering. They are plotted as star and crossed circle symbols in Fig. 6, matching with our measured data. For comparison, the $\langle u^2_{Si-O}\rangle$ and $\langle u^2_{O-O}\rangle$ values of cristobalite crystal determined by total scattering [32] are plotted as the hexagon symbols in Fig. 6. The $\langle u^2_{Si-O}\rangle$ and $\langle u^2_{O-O}\rangle$ values for the crystal are systematically lower than the corresponding values for the glass. This is because the atom pair-distance deviation, $<u^2_{ij}>^{1/2}$, for the glass is caused by both static disorder and thermal vibration, while the value for the crystal results predominantly from thermal vibrations only. The difference between crystal and glass for $\langle u^2_{O-O}\rangle$ is larger than that for $\langle u^2_{Si-O}\rangle$. This is also expected because the bond-length variation of Si-O atom pairs only contains the stretching mode, which is the length change along the bond direction; in contrast, the pair distance deviation of O-O atom pairs contains both stretching and weaker angular modes. Our FS data, in line with reported values, indicate that the *I(Q)*-fitting method produces accurate values of $\langle u^2_{ij}\rangle$, which will provide important through-T_g structural-change information for silicate glasses.

3.3. . Method II: refined RingFSDP for medium-range – ring-structural changes

3.3.1. . Refined RingFSDP method

We recently developed a method, RingFSDP, to quantify the ring-size distribution of silicate glasses from the FSDP of the neutron-scattering structure factor [16]. The FSDP can be deconvoluted into three Gaussian peaks with fixed positions using a Fourier transformation – fitting – back-Fourier transformation method. Since a Gaussian peak is defined by three parameters, position, height and width, a total of nine parameters is needed for deconvolution of the FSDP into three individual peaks. However, nine variables are too much for a reliable fitting. Therefore, we fix the three position values, which are derived from the mean values of 80 fittings, and only refine six parameters (three heights and three widths). The real space representation *I(r)* of FSDP can be fitted by Eq. (3):

$$\begin{aligned} I(r) &= A_1 \times \mathbf{exp}\left[-\left(\frac{r}{\lambda_1}\right)^{\beta}\right] \\ &\times \sin\left(\frac{2\pi}{r_1}\times r\right) + A_2 \times \mathbf{exp}\left[-\left(\frac{r}{\lambda_2}\right)^{\beta}\right] \\ &\times \sin\left(\frac{2\pi}{r_2}\times r\right) + A_3 \times \mathbf{exp}\left[-\left(\frac{r}{\lambda_3}\right)^{\beta}\right] \times \sin\left(\frac{2\pi}{r_3}\times r\right) \end{aligned} \quad (3)$$

where A_1, A_2 *and* A_3 are the amplitudes, λ_1, λ_2 *and* λ_3 are the correlation lengths, $\beta = 2.33$, and three constant periodicities (r_1, r_2 and r_3) are fixed as *3.15, 3.70* and *4.30* Å, respectively.

Each peak is ascribed to a certain-sized ring and its integrated area is proportional to the absolute number of such specified size rings. The relative ring-size distribution (f_n) is calculated from the ratio of the integrated peak area ($I_{S_n(Q)}$) to the total FSDP area ($I_{S_{FSDP}(Q)}$) using Eq. (4):

$$f_n = \frac{I_{S_n(Q)}}{I_{S_{FSDP}(Q)}} \quad (4)$$

Then, the average medium-range distance can be calculated using Eq. (5):

$$\begin{aligned} Average\ medium-range\ distance_{RT} &= \mathbf{f}_{\le 4ring} \times 3.145 + f_{5ring} \times 3.70 \\ &+ f_{\ge 6ring} \times 4.30 \end{aligned} \quad (5)$$

where f_n is the relative ring size distribution, the three fixed *r*-values of 3.145, 3.70, and 4.30 Å being derived experimentally from the fitting of 80 glass data-sets measured at room temperature [16].

For a glass measured at a non-ambient temperature, the basic building block, the SiO_4 tetrahedron, expands, as shown in Fig. 5. A ring

Table 1
Refinement description of refined RingFSDP method.

Refinement	Position (r)	Amplitude (A)	Correlation length (λ)	Purpose
First	Fixed by RT values	Refined	Refined	Determine medium-range distance expansion factor α_T
Second	Refined using constraint α_T	Refined	Refined	Ring structure evolution

formed by tetrahedra should also expand, which means that the three fixed positions should also increase accordingly. However, as discussed above, a direct refinement of a total of nine parameters (three positions, three heights and three widths) does not lead to a reliable fitting. Instead, we modify the RingFSDP method with a two-step refinement – the Refined RingFSDP method, as summarized in Table 1.

First, we apply the original RingFSDP method by refining six height and width parameters with three fixed positions. Even though this is not physically correct, our goal is to determine the average medium-range distance at that specified temperature (*Average medium-range distance*$_T$) using Eq. (5). Then, we can calculate the average medium-range distance expansion factor α_T by referencing the average medium-range distance at RT using Eq. (6):

$$\alpha_T = Average\ medium - range\ distance_T / Average\ medium - range\ distance_{RT} \quad (6)$$

We then carry out a second refinement with three expanded *r*-positions refined around $r \times \alpha_T$ by a constraint of ± 0.01. Good fits are achieved for all 16 diffraction patterns measured at different temperatures with a reduced mean-square-error $\chi^2 < 1.0 \times 10^{-4}$. Fig. 7(a) shows the zoomed *S(Q)* FSDP overlay of RT and 950 °C glass data. In addition to the peak-area decrease, the other change of note is that the FSDP shape skews more in the high-*Q* part for the 950 °C pattern. The FSDP deconvolution results for RT and 950 °C data are plotted in Fig. 7(b) and (C). For each data-set, three individual peaks are plotted; the sum (dotted green curve) is in fair agreement with the experimental *I(r)* (solid curve).

The absolute integrated peak area of $S_n(Q)$ back-Fourier

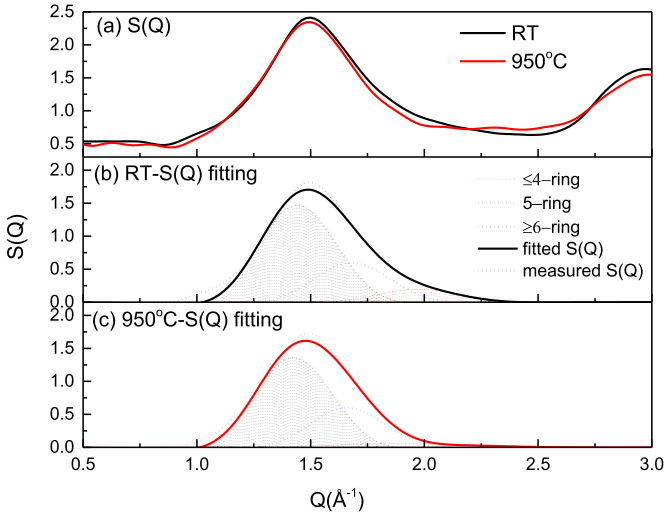

Fig. 7. Room-temperature and 950 °C FSDP and their fitting for FS. (a) Zoomed *S*(*Q*)-FSDP of RT (black) and 950 °C (red); (b) & (c) RT and 950 °C deconvolution of the FSDP by Refined RingFSDP. Three periodicities of the RT pattern were fixed to the values of 3.145, 3.70, and 4.30 Å. For the 950 °C data-set, three periodicities were refined to 3.158, 3.732, and 4.344 Å in response to thermal expansion. Comparing the RT to the 950 °C data, the absolute areas ($I_{S_n(Q)}$) of all sized rings decrease with increasing temperature, but the peak area of small size ≤4-ring decreases more rapidly than that of large size rings, leading to the FSDP shape skewing in the high-*Q* part. (For interpretation of the references to color in this figure legend, the reader is referred to the web version of this article.)

transformed from *I(r)* fitting and their relative fraction f_n, *I(r)* fitting parameters correlation length λ_n and periodicity r_n are plotted with temperature in Fig. 8(a)–(d). The average medium-range distance at each *T* can be calculated by Eq. (7):

$$Average\ medium - range\ distance_T = f_{\leq 4ring} \times r_{\leq 4ring} + f_{5ring} \times r_{5ring} + f_{\geq 6ring} \times r_{\geq 6ring} \quad (7)$$

where $f_{n\text{-}ring}$ is the relative ring size distribution defined by Eq. (4) plotted in Fig. 8(b), $r_{n\text{-}ring}$ is the medium-range distance refined with constraint $\alpha_T$and plotted in Fig. 8(d).

The average medium-range distance change with *T*, is plotted in Fig. 8(e) with values shown by left-axis. Its thermal expansion value calculated by $Expansion_T = \frac{r_T - r_{RT}}{r_{RT}}$ is shown by the right-axis of Fig. 8(e). Since the error of average medium-range distance (δ_r) is from the $I_{FSDP}(r)$ deconvolution and fitting, it can be estimated approximately from the fitting merit - *reduced* χ^2 by $\sqrt{\chi^2 \times degree\ of\ freedom}$. Then the error of expansion $\delta_{expansion}$ is calculated as $\sqrt{2} \times \delta_r$ using the division rule of error propagation. The $\delta_{expansion}$ errors are plotted as the vertical bar in Fig. 8(e). Therefore, another local CTE, derived by the linear fitting of expansion data, is 21(2) × 10^{-6} K^{-1} with the errors calculated from the $I_{FSDP}(r)$ fitting result as discussed above. As explained earlier, the *F(Q)* statistic error is not propagated during the CTE error calculation. This medium-range CTE is more than two times higher than short-range CTE as 9.1(9) × 10^{-6} K^{-1}. The significant CTE difference between two distance ranges reflects glass-structure changes within the "rigid-unit mode" model, where each tetrahedron behaves as a rigid unit with low short-range CTE and the flexible rotations between rigid units lead to high medium-range CTE.

As shown in Fig. 8(a)–(d), the most significant structural change is the correlation length of ≤ 4-membered ring λ_4 which drops significantly as temperature increases. This is also reflected by the significant area drop of ≤ 4-ring for 950 °C glass compared to RT, as shown in Fig. 7(b) and (c). The structural evolution derived from area and shape changes are illustrated in the next two sections.

3.3.2. . FSDP-area decrease

In-situ neutron [19,20] and X-ray [21,22] total-scattering measurements of fused silica show that the peak area of the first sharp diffraction peak (FSDP) decreases with increasing temperature. In agreement with earlier studies that show a 10% FSDP intensity drop from 25 to 1036 °C [20], our data show that the integrated FSDP-area decreases by 9% at 950 °C relative to the room-temperature (RT) value. It is quite common in crystals with rigid polyhedral building blocks – e.g., a molecular crystal, such as CCl_4 – that the local structure of the building block deforms very little relative to the motions of the building blocks relative to each other. While the 'molecular' building blocks, the SiO_4 tetrahedra, are not completely decoupled in fully networked SiO_2, it is reasonable to assume, and is shown in the following, that the relative motion of the building blocks is the main reason for the decrease in the intensity of the FSDP.

In our recently developed method (RingFSDP) [16], the FSDP of a silicate glass can be deconvoluted into three components, each attributed to different numbers of ring members. Adopting the general intensity expression for Bragg peaks [33], the FSDP area (I_{FSDP}) can be simplified as Eq. (8):

$$I_{FSDP} = \sum [A\ N_{n-rings}\ |B_{n-rings}|^2 \exp(-Q^2_{n-rings}\langle u^2_{n-rings}\rangle/2)] \quad (8)$$

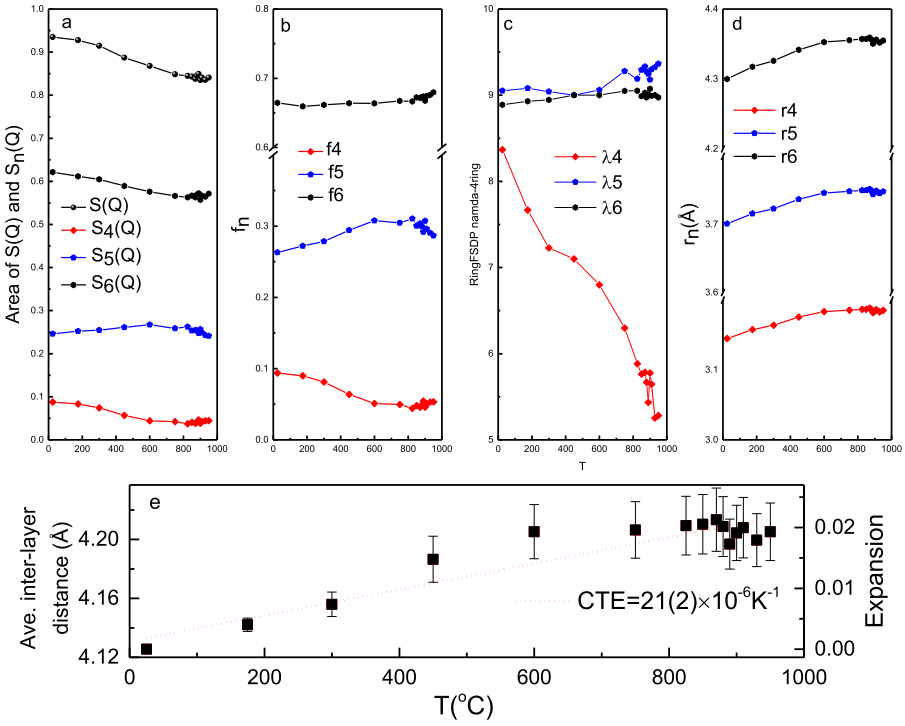

Fig. 8. Deconvolution results obtained by the Refined RingFSDP method and the average medium-range distance change with *T*. (a) Absolute integrated peak area of *S(Q)* and its three deconvoluted peaks; (b) The relative ring-size distribution; (c) Correlation length λ; (d) The refined *r*-values constrained by the ring-expansion factor α. The fitting errors in plot (a) to (d) are smaller than symbol size. (e) The average medium-range distance change (left-axis) and its expansion (right-axis) with *T*, the vertical bars represent the expansion errors by $I_{FSDP}(r)$ fitting. The CTE slope (red dot line) is determined by a linear fitting of expansion data weighted by the $I_{FSDP}(r)$ fitting error.

where *A* is a scale factor related to the instrument configuration and should be 1 for a normalized S(Q); $N_{n\text{-}rings}$ represents the number of *n*-membered rings; $B_{n\text{-}rings}$ is the neutron- scattering length of *n*-membered rings, and is dependent on the composition but it cannot be calculated due to the unclear nature of atomic-pair contributions to the FSDP; $\exp(-Q^2_{n-rings}\langle u^2_{n-rings}\rangle/2)$ is the Debye-Waller (DW) factor, with $\langle u^2_{n-rings}\rangle$ being the mean-squared medium-range distance variation of *n*-membered rings.

Eq. (8) can be further simplified to Eq. (9) by using an average scattering length and DW factor:

$$I_{FSDP} = A\,|B_{ave.}|^2 \exp(-Q^2_{ave.}\langle u^2_{ave.}\rangle/2) \times \sum N_{n-rings} \tag{9}$$

For the same glass measured by the same configuration, the *A* and $B_{ave.}$ terms in Eq. (9) are constants. It is very unlikely that the total ring number ($\sum N_{n-rings}$) can change for a glass below the T_g, as that would require the breaking and reconnection of Si-O bonds. Then, we should be able to calculate the FSDP intensity ratios (I_{950}/I_{RT}) using Eq. (10):

$$\frac{I_{950}}{I_{RT}} = \frac{\exp\left(-\frac{Q^2_{950\ ave.}\langle u^2_{ave.}\rangle_{950}}{2}\right)}{\exp\left(-\frac{Q^2_{RT\ ave.}\langle u^2_{ave.}\rangle_{RT}}{2}\right)} \approx \exp(-Q^2_{RT\ ave.}(\langle u^2_{ave.}\rangle_{950} - \langle u^2_{ave.}\rangle_{RT})/2) \tag{10}$$

With a value $\frac{I_{950}}{I_{RT}} = 0.91$, and an RT-FSDP position of $Q = 1.495$ Å^{-1}, the difference of mean-squared atom pair distance deviations between RT and 950 °C ($\langle u^2_{ave.}\rangle_{950} - \langle u^2_{ave.}\rangle_{RT}$) is 0.0844 Å^2, whose correctness can be checked by comparison with $\langle u^2\rangle_{950} - \langle u^2\rangle_{RT}$ values of short-range Si-O and O-O atom pairs. As shown in Table 2, as *T* increases from RT to 950 °C, the short-range Si-O atom pairs expand by 0.85%, with $\langle u^2_{Si-O}\rangle$ increasing by 0.0029 Å^2, whereas O-O atom pairs expand by 0.80%, with $\langle u^2_{O-O}\rangle$ increasing by 0.0111 Å^2. The medium-range average medium-range distance, calculated from Eq. (7) in the next section, expands by 1.84%, which is about twice that of the short-range expansion. But its $\langle u^2_{n-rings}\rangle$ value increases by 0.0844 Å^2, which is 29 times that of the $\langle u^2_{Si-O}\rangle$ increase, and 7.6 times that of the $\langle u^2_{O-O}\rangle$ increase. Based on the unphysically large $\langle u^2_{n-rings}\rangle$ increase, we conclude that Eq. (10) is incomplete, and the assumption of a constant total ring number ($\sum N_{n-rings}$) might need to be reconsidered.

Table 2
Short- and medium-range distance (Å) and $\langle u^2\rangle$ (Å^2) changes for FS between RT and 950 °C.

Correlation scale	Length (Å)			$\langle u^2\rangle$ (Å^2)		
	RT	950 °C	Expansion[1] (%)	RT	950 °C	Diff. (950 °C-RT)
Si-O	1.603	1.616	0.85	0.0020	0.0049	0.0029
O-O	2.619	2.640	0.80	0.0061	0.0172	0.0111
Ave. medium-range distance[2]	4.127	4.203	1.84	NA	NA	0.0844

[1] $Expansion = \frac{r_{950°C} - r_{RT}}{r_{RT}} \times 100\%$

[2] Average medium-range distance calculation is described in Section 3.3.1 using Eq. (7).

First, let us look how the rings can contribute to constructive diffraction leading to the FSDP. A real-reciprocal space analysis, combining a continuous wavelet-transform analysis and molecular-dynamics simulations, has demonstrated that the medium-range-order-related FSDP in FS is manifested by interatomic distances in the region of $r \sim 5$ Å, associated with a couple of local "pseudo-Bragg" planes [34]. Such near-parallel local "planes" are formed by both Si and O atoms from the second-nearest neighbors. The perpendicular distance between the parallel planes will result in constructive diffraction, leading to the FSDP in *S(Q)*. Small-size rings will exhibit shorter distances between planes while larger-sized rings will correspond to longer distances. Only near-parallel planes will contribute to the FSDP. If a ring has a shape that is too skewed or distorted from the averaged ring shape, it will not contribute significantly to the FSDP, even if the ring itself is still intact. Therefore, we need to add a ring-shape factor, $Shape_{n\text{-}rings}$, to Eq. (9) which leads to Eq. (11):

$$I_{FSDP} = A\,|B_{ave.}|^2 \exp(-Q^2_{ave.}\langle u^2_{ave.}\rangle/2) \times \sum (Shape_{n-rings} \times N_{n-rings}) \tag{11}$$

where the ring-shape factor, $Shape_{n\text{-}rings}$, takes values from *0* to *1*. For same-sized rings, if their shapes are all within a given shape range, the

corresponding S_{rings} value is 1, indicating that all the rings contribute to the FSDP. As the temperature increases, some ring shapes can get distorted by flexible Si-O-Si-angle rotations; those rings still exist but will not contribute significantly to the FSDP. The ring shape factor will decrease to $Shape_{n\text{-}ings} = 1\text{-}N_{distorted\ n\text{-}rings}/N_{total\ n\text{-}rings}$. The ring-shape factor concept is introduced to explain the FSDP-area decrease and shape change; an MD-simulation study is underway to verify this and will be reported separately.

The FSDP decrease with increasing temperature for silicate glasses is opposite to the behavior exhibited by chalcogenide glasses [35]. Unlike network silicate glasses with ring structures, chalcogenide glasses have layered structures and their FSDPs correspond to medium-range separations. As T increases, the intra-layer structure become more disordered due to thermal vibrations, resulting in smoother layers and a more ordered medium-range structure, giving an increased FSDP area. The different temperature behaviors reflect a different origin of the FSDP.

While we have experimentally demonstrated the FSDP-area decrease with increasing temperature, simulations can generate glass structures with an order-of-magnitude higher change. Sodium silicate glass models [$(Na_2O)_{30}(SiO_2)_{70}$] derived by MD simulations with different cooling rates [36] can be used to further prove the FSDP-area decrease for more disordered glass structures. Glass models, cooled at faster rates, have a larger degree of disorder which corresponds to our high-T glass structure. As shown in Fig. 9, the FSDP area of a rapidly cooled glass model (100 K/ps) drops by 32% compared to that of a slowly cooled glass model (0.01 K/ps), while the total ring number only decreased by 5% as counted by the RINGS package [37]. We propose that the decrease can be attributed to a ring-shape change.

3.3.3. . FSDP-shape change

As shown in Fig. 8(a), the absolute amounts of all sizes of rings ($I_{S_n(Q)}$) contributing to the FSDP decrease as the temperature increases, which is in line with the $Shape_{n\text{-}rings}$ factor of Eq. (11) changing, as proposed in the previous section. The small-sized rings decrease more rapidly than the large-sized rings, indicating that small-sized rings are more sensitive in responding to temperature changes. This finding is supported by MD simulations of $(Na_2O)_{30}(SiO_2)_{70}$ glasses showing that the small rings are mechanically unstable and experience internal stress/strain, so their existence is the driving force for the structural relaxation of silicate glasses [38]. This also qualitatively explains why the FSDP shape skews more in the high-Q part which corresponds to the small-ring component. Again, the change of the absolute amount of rings does not mean that rings decompose on heating. Structural changes below T_g should only belong to a low-energy deformation type. The external energy provided by heating is not large enough to overcome the high energy barrier necessary to break or switch a bond; instead, the structure changes in a spatially cooperative manner through torsional motion of SiO_4 tetrahedra via Si-O-Si flexible rotations. This is reflected as a ring-shape change referenced to the average ring shape detected by the neutron $S(Q)$. The ring-shape change with temperature is revealed by an RMC simulation of the quartz α→β phase transition [13], as well as MD simulation of the cristobalite α→β phase transition [39]. Based on the model that the FSDP results from scattering from near-parallel planes [34], we hypothesize that such distorted, out-of-shape buckled rings do not contribute significantly to the FSDP, leading to a decrease of the FSDP area.

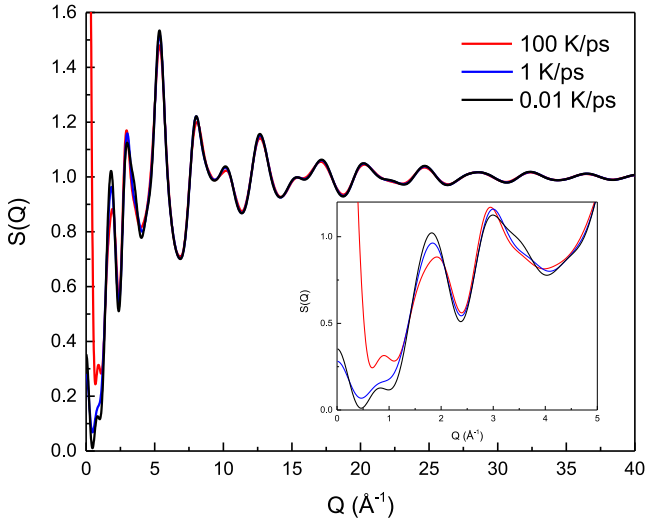

Fig. 9. MD-simulated neutron structure factor $S(Q)$ of $(Na_2O)_{30}(SiO_2)_{70}$ glass prepared with different cooling rates [36]. Three glass models show similar high-Q range (3rd peak and higher) features, indicating the same short-range order. In contrast, the medium-range order changes significantly with changes in cooling rate; as shown in the insert, the FSDP area decreases significantly with increasing cooling rate.

4. Conclusion

In conclusion, we have used a well-developed technique – *in-situ* neutron total scattering – to recheck a well-studied, prototypical glass, fused silica. We propose the SiO_4 rigid unit as the structural origin of low-temperature structure changes. This is supported by the "Rigid Unit Mode" behavior observed from the FS structural change with temperature. As shown in Fig. 10(a), the similar slopes of the relative distance deviation ($\langle u_{ij}^2 \rangle^{(1/2)}/r$) for Si-O and O-O atom pairs with T demonstrate the uniform tetrahedral expansion of SiO_4 units, while in Fig. 10(b), flexible Si-O-Si rotation is reflected by the fact that the expansion of the medium-range units (characterized by a CTE of $21(2) \times 10^{-6}\ K^{-1}$) is more than two times higher than that of the short-range Si-O tetrahedra units (characterized by a CTE of $9.1(9) \times 10^{-6}\ K^{-1}$). Since the macro-scale bulk CTE of FS is $0.55 \times 10^{-6}\ K^{-1}$ [40], we note that the short-range and medium-range local CTEs are 15 and 39 times higher than the macroscopic bulk CTE, respectively. The significant discrepancy between local and bulk CTEs should not be surprising since there is no physical reason to expect they are same. As philosophically illustrated by Egami and Billinge to emphasize the difference between local (microscopic) and global (macroscopic) views of material structure [41], they are like national statistics and personal reports in describing an event such as a war between nations. Here, taking event as the heating of a FS glass, we observe that local (short and medium-range CTEs) and, global views (as dilatometry-measured bulk CTE) indeed exhibit a striking discrepancy. To reach the low bulk CTE of FS, there must be some contracting structural features compensating the positive local expansions. For example, very low or even negative bulk CTEs are commonly observed in crystalline silicate materials with open-frameworks, such as cordierite ($Mg_2Al_3Si_5O_{18}$) [42] and β-eucryptite ($LiAlSiO_4$) [43]. Their bulk negative CTEs originate from the anisotropic thermal expansion with positive values (expansions) in two unit-cell directions compensated by negative values (contractions) in the third direction. We propose that ring shape distortions and the ring-network reorganizations may explain the low bulk CTE of glassy silica. MD simulations might be a way to confirm it.

Although this is the first time that the discrepancy between local short and medium-range and bulk CTE is qualitatively reported for FS, this behavior is not a specific to silicate glasses but has also been reported in the case of a polybutadiene polymer [44], where the local CTE obtained from the main-peak position of $S(Q)$ is smaller than the dilatometry-determined bulk CTE. A similar discrepancy is also observed in crystalline α-quartz, wherein the local CTE derived from the Si-O bond length is $2.2(4) \times 10^{-6}\ K^{-1}$ [29], whereas the bulk CTE is $15 \times 10^{-6}\ K^{-1}$ [45].

Our data show that flexible rotations of Si-O-Si linkages between SiO_4 rigid units occur through the whole temperature range. The nearest tetrahedra rearrangements lead to ring-shape changes in the

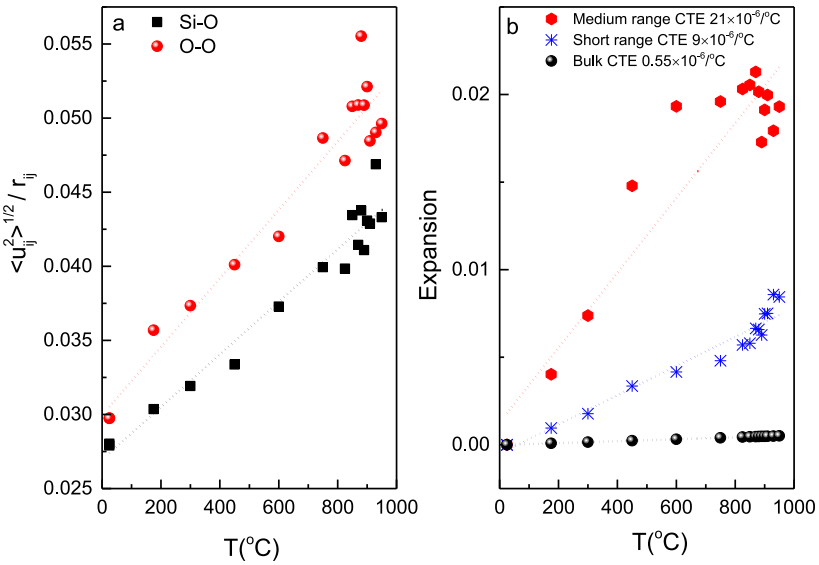

Fig. 10. The "Rigid-unit mode" behavior of FS structural change with temperature. (a) The behavior of SiO_4 rigid units is shown by the similar slopes of the relative distance deviation ($\langle u_{ij}^2 \rangle^{(1/2)}/r$) for Si-O and O-O atom pairs with T, indicating uniform tetrahedron expansion; (b) Flexible Si-O-Si rotation is reflected by the two times higher medium-range distance expansion in comparison with short-range Si-O tetrahedra expansion, in comparison with the bulk CTE [40].

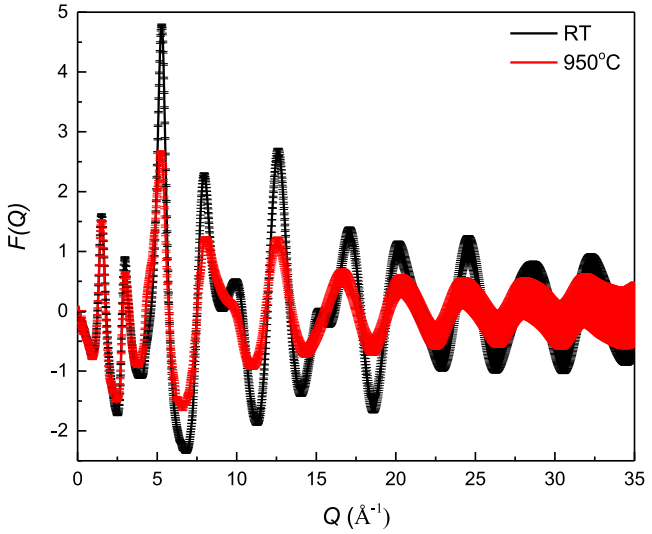

Extended Data Fig. 1. Reduced structure factor functions, $F(Q)$, measured at RT and 950 °C. The vertical bars represent the measured data points with statistical errors.

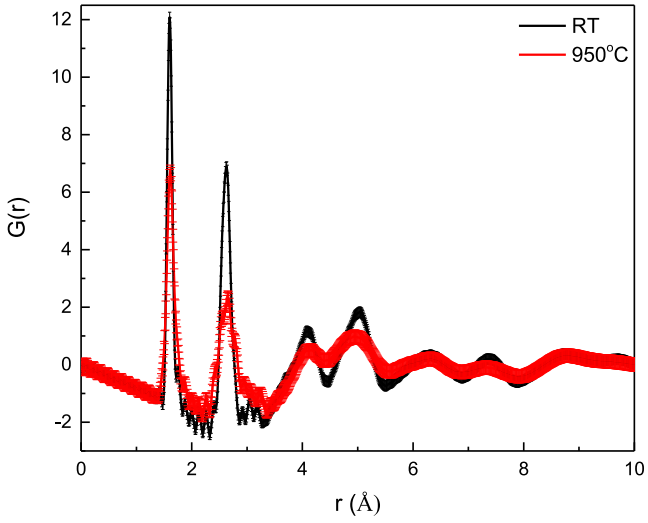

Extended Data Fig. 2. Reduced pair distribution functions $G(r)$ obtained by Fourier transformation with $Q_{max} = 50$ Å^{-1} measured at RT and 950 °C. The vertical bars represent the propagation errors by Fourier transform.

medium range. This is reflected by subtle but real changes of the first sharp diffraction peak (FSDP) in the structure factor. The ring-structure evolution with temperature is quantified using the Refined RingFSDP method. This answers "how does glass relax at low-T?", and it will be complemented by a study of structural changes through the glass transition for other silicate glasses. This method paves the way to measure the structural change of other silicate glasses, especially through T_g, to shine light on low-temperature relaxation phenomena in glasses.

Code availability

Two Python programs were developed for the data analysis. Tetrahedron Expansion was developed to batch-process $F(Q)$ files to obtain $I(Q)$ of Si-O and O-O atom pairs and then profile-fit $I(Q)$. Refined RingFSDP batch-processes $F(Q)$ files for two-step refinements: acquire $I(r)$ for the FSDP, profile-fit $I(r)$ with fixed r, then calculate the ring-expansion factor α, profile-fit $I(r)$ with the expanded $r \times \alpha$, inverse Fourier transform to get $F_n(Q)$, derive $S_n(Q)$ and integrate for ring-size distribution calculations. The code is available from the NOMAD beamline of ORNL upon request.

Data availability

The datasets generated and analyzed of this study are available from the corresponding author upon request.

CRediT authorship contribution statement

Ying Shi: Conceptualization, Methodology, Formal analysis, Writing - original draft. **Dong Ma:** Data curation, Formal analysis, Writing - review & editing. **Albert P. Song:** Software. **Bryan Wheaton:** Formal analysis, Writing - review & editing. **Mathieu Bauchy:** Formal analysis, Writing - review & editing. **Stephen R. Elliott:** Formal analysis, Writing - review & editing.

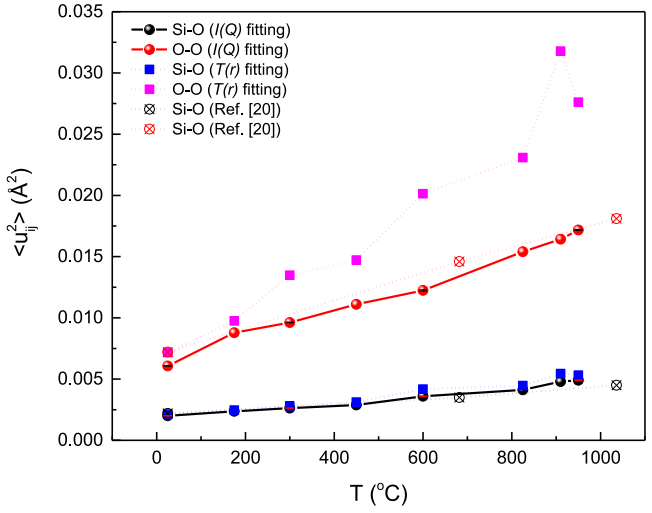

Extended Data Fig. 3. Mean-square atom pair distance deviation $\langle u^2 \rangle$ change with temperature of FS derived from total scattering. The Si-O pairs are shown in black and O-O in red color. The $\langle \boldsymbol{u}^2_{Si-O} \rangle$ (black ball) and $\langle \boldsymbol{u}^2_{O-O} \rangle$ (red ball) are derived from the $I_{Si\text{-}O}(Q)$ and $I_{O\text{-}O}(Q)$ fitting, with error bars shown for four temperatures. The $\langle \boldsymbol{u}^2_{Si-O} \rangle$ (blue square) and $\langle \boldsymbol{u}^2_{O-O} \rangle$ (pink square) are derived from direct fitting of $T_{Si\text{-}O}(r)$ and $T_{O\text{-}O}(r)$. The reported in-situ FS plotted by crossed circles are from [20]. (For interpretation of the references to color in this figure legend, the reader is referred to the web version of this article.)

Declaration of Competing Interest

The authors declare that they have no known competing financial interests or personal relationships that could have appeared to influence the work reported in this paper.

Acknowledgments

Neutron measurements used resources at the Spallation Neutron Source, a DOE Office of Science User Facility operated by the Oak Ridge National Laboratory. Many thanks are owed to Jörg Neuefeind and Michelle Everett for technical assistance at NOMAD and Daniel Olds (formerly at ORNL) for the Python algorithm for Fourier transformation. Y. S. is grateful for constructive comments from Oliver Alderman of Materials Development Inc., and to Ozgur Gulbiten of Corning Inc. for preparing the FS rod sample. M. B. acknowledges funding provided by the National Science Foundation under Grant no. 1928538.

References

[1] O. Gulbiten, J.C. Mauro, X. Guo, O.N. Boratav, Viscous flow of medieval cathedral glass, J. Am. Ceram. Soc. 101 (2018) 5–11.
[2] Y. Yu, M. Wang, M.M. Smedskjaer, J.C. Mauro, G. Sant, M. Bauchy, Thermometer effect: origin of the mixed alkali effect in glass relaxation, Phys. Rev. Lett. 119 (2017) 095501.
[3] N.W. Taylor, B. Noyes, Aging thermometers, J. Am. Ceram. Soc. 27 (2) (1944) 57.
[4] R.C. Welch, J.R. Smith, M. Potuzak, X. Guo, B.F. Bowden, T.J. Kiczenski, D.C. Allan, E.A. King, A.J. Ellison, J.C. Mauro, Dynamic of glass relaxation at room temperature, Phys. Rev. Lett. 110 (2013) 265901.
[5] J.W. Berthold, S.F. Jacobs, M.A. Norton, Dimensional stability of fused silica, Invar, and several ultralow thermal expansion materials, Appl. Opt. 15 (8) (1976) 1898.
[6] B. Ruta, G. Baldi, Y. Chushkin1, B. Ruffle, L. Cristofolini, A. Fontana, M. Zanatta, M. Nazzani, Revealing the fast atomic motion of network glasses, Nat. Commun. (2014) 3939.
[7] A.P. Giddy, M.T. Dove, G.S. Pawley, V. Heine, The determination of rigid unit modes as potential soft modes for displacive phase transitions in framework crystal structures, Acta Crystallogr. A49 (1993) 697–703.
[8] K.D. Hammonds, M.T. Dove, A.P. Giddy, V. Heine, B. Winkler, Rigid unit phonon modes and structural phase transitions in framework silicates, Amer. Mineral. 81 (1996) 1057–1059.
[9] K.O. Trachenko, M.T. Dove, K.D. Hammonds, M.J. Harris, V. Heine, Low energy dynamics and tunneling states in silica glass, Phys. Rev. Lett. 81 (1998) 3431–3434.
[10] M.T. Dove, K.D. Hammonds, M.J. Harris, V. Heine, D.A. Keen, A.K.A. Pryde, K.O. Trachenko, M.C. Warren, Amorphous silica from the rigid unit mode approach, Mineral. Mag. 64 (2000) 377–388.
[11] E.J. Palin, K.O. Trachenko, M.T. Dove, Computer simulation study of low-energy excitations of silicate glasses, J. Phys. Condens. Matter 14 (2002) 4857–4879.
[12] M.T. Dove, M.J. Harris, A.C. Hannon, J.M. Parker, I.P. Swainson, M. Gambhir, Floppy modes in crystalline and amorphous silicates, Phys. Rev. Lett. 78 (1997) 1070–1073.
[13] M.G. Tucker, D.A. Keen, M.T. Dove, A detailed structural characterization of quartz on heating through the a-b phase transition, Mineral. Mag. 65 (2001) 489–507.
[14] U. Buchenau, N. Nucker, A.J. Dianoux, Neutron scattering study of the low-frequency vibrations in vitreous silica, Phys. Rev. Lett. 53 (1984) 2316–2319.
[15] S.V. Nemilov, Physical ageing of silicate glasses at room temperature: general regularities as a basis for the theory and the possibility of a priori calculation of the ageing rate, Glass Phys. Chem. 26 (2000) 511–530.
[16] Y. Shi, J. Neuefeind, D. Ma, K. Page, L.A. Lamberson, N.J. Smith, A. Tandia, A.P. Song, Ring size distribution in silicate glasses revealed by neutron scattering first sharp diffraction peak analysis, J. Noncryst. Solids 516 (2019) 71–81.
[17] J. Neuefeind, M. Feygenson, J. Carruth, R. Hoffmann, K. Chipley, The nanoscale ordered materials diffractometer NOMAD at the spallation neutron source SNS, Nucl. Instrum. Methods Phys. Res. Sect. B 287 (2012) 68–75.
[18] Y. Shi, N.T. Lonnroth, R.E. Youngman, S.J. Rzoska, M. Bockowski, M.M. Smedskjaer, Pressure-induced structural changes in titanophosphate glasses studied by neutron and X-ray total scattering analyses, J. Noncryst. Solids 483 (2018) 50–59.
[19] B. Graneli, U. Dahlborg, The vibrational motions in vitreous silica at high temperatures, J. Noncryst. Solids 109 (1989) 295.
[20] S. Susman, K.J. Volin, D.G. Montague, D.L. Price, Temperature dependence of the first sharp diffraction peak in vitreous silica, Phys. Rev. B 43 (1991) 11076.
[21] Q. Mei, C.J. Benmore, J.K.R. Weber, Structure of liquid Sio_2: a measurement by high-energy X-ray diffraction, Phys. Rev. Lett. 98 (2007) 057802.
[22] L.B. Skinner, C.J. Benmore, J.K.R. Weber, M.C. Wilding, S.K. Tumber, J.B. Parise, A time resolved high energy X-ray diffraction study of cooling liquid Sio_2, Phys. Chem. Chem. Phys. 15 (2013) 8566.
[23] L. Cormier, G. Calas, B. Beuneu, Structural changes between soda-lime silicate glass and melt, J. Noncryst. Solids 357 (2011) 926–931.
[24] D.A. Keen, A comparison of various commonly used correlation functions for describing total scattering, J. Appl. Cryst. 34 (2001) 172–177.
[25] A.C. Hannon, Neutron diffraction techniques for structural studies of glasses, Modern Glass Characterization, Wiley, Hoboken, 2015, p. 195.
[26] A.C. Hannon, Neutron diffraction techniques for structural studies of glasses, Modern Glass Characterization, Wiley, Hoboken, 2015, p. 198.
[27] G. Knott, R. Shrager, On-line modeling by curve-fitting, Proceedings of the 1972 SIGGRAPH Seminar on Computer Graphics in Medicine, Pittsburgh,Pennslyvannia, 1972, pp. P138–P151.
[28] R.T. Downs, G.V. Gibbs, K.L. Bartelmehs, M. Boisen, Variations of bond lengths and volumes of silicate tetrahedra with temperature, Am. Mineral. 77 (1992) 751–757.
[29] M.G. Tucker, M.T. Dove, D.A. Keen, Direct measurement of the thermal expansion of the Si-O bond by neutron total scattering, J. Phys. Condens. Matter 12 (2000) 425–430.
[30] O. Majerusa, L. Cormier, G. Calas, B. Beuneu, A neutron diffraction study of temperature-induced structural changes in potassium disilicate glass and melt, Chem. Geol. 213 (2004) 89–102.
[31] A.C. Wright, R.N. Sinclair, Neutron scattering from vitreous silica III. Elastic diffraction, J. Noncryst. Solids 76 (1985) 351–368.
[32] M.T. Dove, D.A. Keen, A.C. Hannon, I.P. Swainson, Direct measurement of the Si–O bond length and orientational disorder in the high-temperature phase of cristobalite, Phys. Chem. Miner. 24 (1997) 311–317.
[33] R. Jenkins, R.L. Snyder, Introduction to X-ray Powder Diffractometry, Wiley, New York, 1996.
[34] T. Uchino, J.D. Harrop, S.N. Taraskin, S.R. Elliott, Real and reciprocal space structural correlations contributing to the first sharp diffraction peak in silica glass, Phys. Rev. B 71 (2005) 014202.
[35] L.E. Busse, Temperature dependence of the structures of As_2Se_3 and As_xSi_{1-x} glasses near the glass transition, Phys. Rev. B 29 (1984) 3639–3651.
[36] X. Li, W. Song, K. Yang, N.M. Anoop Krishnan, B. Wang, M.M. Smedskjaer, J.C. Mauro, G. Sant, M. Balonis, M. Bauchy, Cooling rate effects in sodium silicate glasses: bridging the gap between molecular dynamics simulations and experiments, J. Chem. Phys. 147 (2017) 074501.
[37] S. Le Roux, P. Jund, Ring statistics analysis of topological networks: new approach and application to amorphous GeS_2 and SiO_2 systems, Comput. Mater. Sci. 49 (2010) 70–83.
[38] W. Song, X. Li, B. Wang, N.M. Anoop Krishnan, S. Goyal, M.M. Smedskjaer, J.C. Mauro, C.G. Hoover, M. Bauchy, Atomic picture of structural relaxation in silicate glasses, Appl. Phys. Lett. 114 (2019) 233703.
[39] F. Yuan, L. Huang, α-β transformation and disorder in β-cristobalite silica, Phys. Rev. B 85 (2012) 134114.
[40] W.E. Forsythe, Smithsonian Physical Tables, 9th ed., Smithsonian Institution, Washington, D.C., 1964, p. P52.
[41] T. Egami, S.J.L. Billinge, Local view of the strucutre, Underneath the Bragg Peaks, Elsevier, Oxford, 2012, p. P4.
[42] M.A. Son, K.W. Chae, J.S. Kim, S.H. Kim, Structural origin of negative thermal expansion of cordierite honeycomb ceramics and crystal phase evolution with sintering temperature, J. Eur. Ceram. Soc. 39 (2019) 2484–2492.
[43] F.H. Gillery, E.A. Bush, Thermal contraction of -Eucryptite ($Li_2O.Al_2O_3.2SiO_2$) by X-ray and dilatometer methods, J. Am. Ceram. Soc. 42 (1959) 175–177.
[44] B. Frick, C. Alba-Simionesco, K.H. Andersen, L. Willner, Influence of density and temperature on the microscopic structure and the segmental relaxation of polybutadiene, Phys. Rev. E 67 (2003) 051801.
[45] G.H. Beall, Industrial applications of silica. Silica: physical behavior, geochemistry and materials applications, Rev. Mineral. 29 (14) (1994) 469–506.